


Distinctive characteristics of exciton-phonon interactions in optically driven MoS₂

Yu-Chen Chang , Yu-Chiao Chan, Bipul Das, Jiao-Fang Syue, Hsiang-Chi Hu, Yann-Wen Lan,^{*} and Ting-Hua Lu [†]
Department of Physics, National Taiwan Normal University, Taipei, Taiwan

 (Received 7 February 2024; revised 20 May 2024; accepted 24 June 2024; published 15 July 2024)

Polarized Raman spectroscopy offers the capability to study the interactions between electrons/excitons and phonons in the presence of intervalley scattering within two-dimensional materials. This study explores the relation between phonon symmetry and exciton-phonon interactions in monolayer and bilayer MoS₂ using polarization-resolved photoluminescence and Raman spectroscopy. The resonant second-order Raman spectra in MoS₂ are closely tied to material properties and laser excitation energy. Experimental and numerical analyses systematically examined phonon symmetry in Raman scattering, revealing a strong correlation between phonon symmetry and spin-valley polarization, especially under resonant excitation. Resonant excitation changed Raman scattering polarization because of the dominant Fröhlich interaction. The strong spin-orbit coupling in monolayer MoS₂ unaffected by thermal vibrations at low temperatures leads to a notable increase in the valley polarization resulting from the restricted energy-level distribution of electron transitions. This phenomenon significantly influences the b mode in second-order resonant Raman scattering, consequently altering the chirality of phonon vibrations. We further propose a mechanism diagram elucidating the interaction between electrons and excitons of intervalley scattering. The study highlights the interplay between electron transitions and phonon-related behaviors in MoS₂, emphasizing the significance of electron/exciton-phonon interactions under varying excitation energies and temperatures. These insights hold crucial implications for the optoelectronic applications of MoS₂.

DOI: [10.1103/PhysRevMaterials.8.074003](https://doi.org/10.1103/PhysRevMaterials.8.074003)

I. INTRODUCTION

The excellent optoelectronic properties of molybdenum disulfide (MoS₂) and other transition metal dichalcogenides (TMDs) have positioned them as leading semiconductor materials in recent years [1–4]. However, the electronic properties of these materials are significantly influenced by electron-phonon interactions. Current research strategies encompass a variety of approaches, such as gating [5–10], doping [11–14], thermal effect [15–18], and optical control [19–21] to explore the interactions of these quasiparticles. The second-order Raman spectra observed in MoS₂ and other TMDs exhibit a wide range of distinct features. These characteristics are closely intertwined with the material's properties and the specific laser energy employed for excitation. Previous investigations into two-dimensional (2D) MoS₂ centered around the examination of the second-order Raman bands using various combinations of laser excitation energies, material thicknesses, and dielectric substrates [22].

Double-resonance Raman (DRR) stands as a unique and valuable second-order process, facilitating the investigation of electron-phonon interactions in MoS₂ [23–27]. By adjusting the incident photon energy, the DRR condition chooses distinct electronic states and pairs of phonons with opposing finite momenta within the Brillouin zone [20]. To date, the unique method of optically spin-polarized excitation and

detection applied onto DRR condition remains unexplored. This approach offers the opportunity to investigate these interactions and electron transitions across different excitation energies, all while considering angular momentum conservation. The comprehensive study of these interactions is essential for uncovering the physical phenomena concealed within the second-order Raman spectra and exciton characteristics of MoS₂.

In this paper, we systematically carried out experimental and numerical analyses aimed at exploring phonon symmetry of both first-order and double-resonance Raman scattering processes in MoS₂ while varying the strength of exciton-phonon coupling. We performed temperature-dependent Raman and photoluminescence (PL) spectroscopy under different polarization and excitation energies of 2.33 eV and 1.96 eV, representing nonresonant and resonant excitations, respectively. The polarized Raman spectrum of MoS₂ exhibits discernible distinctions. We observed changes in the symmetry of degenerate in-plane phonon modes as a result of the modulated exciton-phonon coupling strength, driven by the strengthening of the Fröhlich interaction (FI). The phenomenon of FI arises from the interaction between excitons and longitudinal optical phonons, causing out-of-phase motion of adjacent atoms and generating a macroscopic electric field [28]. Most notably, our analysis, employing spin-polarized excitation and detection, unveiled a correlation between the phonon symmetry and the spin-valley polarization of excitons within the context of DRR scattering. Our study provides a fundamental explanation for the phonon symmetry changes detected by polarization-resolved Raman spectroscopy in monolayer and bilayer MoS₂.

^{*}Contact author: ywlan@ntnu.edu.tw

[†]Contact author: thlu@ntnu.edu.tw

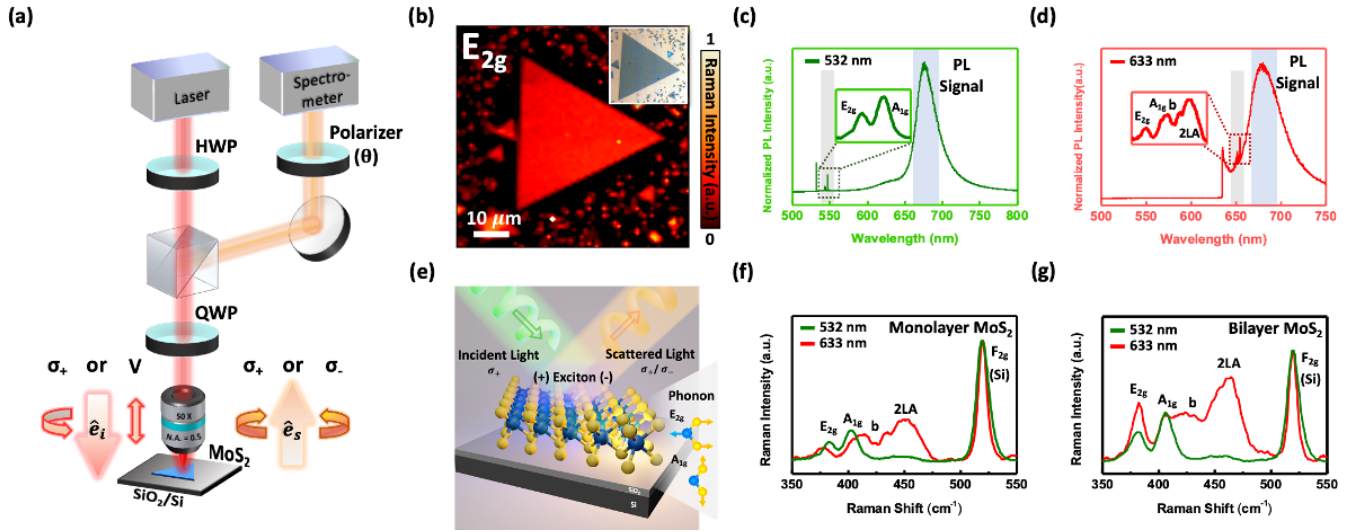


FIG. 1. Experimental setup of PL and Raman spectra of monolayer and bilayer MoS₂ on SiO₂/Si substrate. (a) Schematic diagram of polarization-resolved PL and Raman spectroscopy experimental setup. HWP, half-wave plate; QWP, quarter-wave plate. The arrows indicate the incident and scattered light with different polarization states. (b) Raman intensity mapping of the E_{2g} mode in monolayer MoS₂ with the scale bar of 10 μm. Inset shows the corresponding OM image. (c) PL and Raman signal of monolayer MoS₂ excited by nonresonant (532 nm) and (d) resonant excitation (633 nm). (e) Schematic diagram of the coupling between excitons and phonons with the excitation light. (f) Raman spectra of monolayer MoS₂ and (g) bilayer MoS₂ under nonresonant and resonant excitation.

II. METHODS

A. Sample fabrication

In this paper, a silicon wafer (crystal surface [001]) with 100-nm thick SiO₂ is used as the substrate for the preparation of monolayer MoS₂ and bilayer MoS₂ using chemical vapor deposition. The silicon wafer has been cleaned by sonication in acetone for 10 minutes, followed by isopropanol and deionized water for 5 minutes each before the growth process, and finally dried with a nitrogen gas gun. The growth setup includes the following steps: High-quality powders of MoO₃ (99.99% purity, Sigma-Aldrich) and S (99.99% purity, Sigma-Aldrich) are used as precursor sources in an ambient-pressure CVD system to grow monolayer MoS₂ and bilayer MoS₂ on Si/SiO₂ substrate. A quartz tube with a 3-inch diameter is used as the reaction furnace, which is heated up by three heating coils. During the growth process, a crucible containing 0.3 g of S powder was placed upstream in excess, while a crucible containing 0.011 g of MoO₃ powder is placed at the center of the furnace tube. A target SiO₂/Si with second crucible was placed flat 5 cm behind the MoO₃ source. The tube furnace is continuously filled with highly pure Ar (>99.99%) gas for 500 sccm during the whole growth process. After the filled high purity Ar gas flown in the tube furnace, the tube is heated up at a rate of 25.7 °C/min to the setting temperature at 800 °C and maintained for 10 mins. The S zone started to heat 2 mins before the MoO₃ boat is heated up to 800 °C, and kept between 200–250 °C while the MoO₃ zone maintains the temperature at 800 °C, and then underwent natural furnace cooling to room temperature. The monolayer and bilayer MoS₂ are generated by the reaction, and finally deposited onto the target silicon substrate.

B. Optical measurement

Raman spectroscopy is a fundamental analytical technique widely employed to elucidate the structural, electronic, and

vibrational characteristics of layered materials. Figure 1(a) illustrates an optical setup for temperature-dependent polarized Raman/PL spectroscopy, which utilizes two continuous wave lasers (532 nm and 633 nm), a HWP, and a QWP to enhance measurement precision with the degree of freedom of incident and scattered light. These optical elements are capable of producing linearly or circularly polarized light under nonresonant excitation 532 nm (corresponding to 2.33 eV) and resonant excitation 633 nm (corresponding to 1.96 eV) for the investigation of layered MoS₂. Target samples were focused using a 50X objective lens (numerical aperture, N.A. = 0.5). Polarization-resolved Raman/PL spectra were acquired through the deployment of an adjustable-angle polarizer (with a step of 15° ranging from 0° to 360°) in conjunction with a grating (1200 lines/mm and 150 lines/mm) and a commercial spectrometer (Model: Kymera 328i, Andor). The temperature-dependent investigation of polarization-resolved Raman/PL spectra was conducted by placing the samples in a vacuum chamber (pressure ~1 × 10⁻⁴ torr) and systematically varying the temperature from 77 to 300 K.

III. RESULTS AND DISCUSSION

The schematic experimental arrangement of polarized Raman spectroscopy is depicted in Fig. 1(a). To illuminate the MoS₂ sample, lasers with varying polarizations are controlled using a half-wave plate (HWP) and a quarter-wave plate (QWP) at wavelengths of 532 nm and 633 nm, respectively. With a bandgap of around 1.8 eV in monolayer MoS₂, these two excitation sources, 532 nm (equivalent to 2.33 eV) and 633 nm (equivalent to 1.96 eV), correspond perfectly to the nonresonant and resonant excitation conditions of MoS₂. The PL and Raman signals are captured, and the polarization characteristics are examined using a combination of QWP and polarizer positioned in front of the spectrometer. The

circularly polarized detection of PL and Raman signals provides a new degree of freedom to investigate the physical properties of exciton-phonon coupling in MoS₂. The schematic diagram in Fig. 1(e) illustrates the interaction between excitons and phonons under optical excitation. Exploring how the strength of this coupling affects the correlation between valley polarization and double resonance Raman scattering is a key focus of this study. In Fig. 1(b), the inset shows the optical microscopic (OM) image of the monolayer MoS₂ sample, and the corresponding mapping of the in-plane phonon mode E_{2g} is displayed through the Raman signal intensity. The uniform intensity of the Raman signal indicates the good homogeneity of the material. For the bilayer MoS₂ sample, similar result of uniform intensity distribution can be seen in Fig. S1 within the Supplemental Material (SM) [29].

Figures 1(c) and 1(d) depict the spectra of monolayer MoS₂ excited by 532 nm and 633 nm light sources, including PL and Raman signals. Throughout the subsequent Raman spectroscopy measurements, we meticulously processed the overlapping spectral signals to extract the accurate polarized photoluminescence and Raman spectra. This allowed us to study the underlying representations of excitons and phonons. Figures 1(f) and 1(g) show the Raman spectra of monolayer and bilayer MoS₂, obtained by employing nonresonant and resonant excitation at 532 nm (green curve) and 633 nm (red curve), respectively. In the case of monolayer MoS₂, the optical absorption reveals the major excitonic transitions of A and B excitons as reported in the literature [30]. At 4.5 K, two peaks are assigned to A and B excitons at approximately 1.96 eV and 2.12 eV for MoS₂, and the optical band gap decreases with increasing temperature caused by electron-phonon interactions, a phenomenon explained using the Bose–Einstein model [31]. The optical band gap denotes the energy needed to generate an exciton—a correlated electron-hole pair—via optical absorption across the A and B energy gaps. Therefore, even though the 633 nm (1.96 eV) excitation energy is slightly higher than the optical band gap of MoS₂ (~1.89 eV) at 300 K; it can still be considered fairly close to the resonance condition of the A exciton in MoS₂. At lower temperatures, the optical band gap is closer to 1.96 eV, corresponding to the pronounced resonant condition with the 633 nm (1.96 eV) excitation. Further more, the Raman spectrum of monolayer MoS₂ varies with the energy of the excitation laser source [20]. Experimental results [20] indicate that the resonances of all Raman bands in monolayer MoS₂ coincide with the A and B excitonic transitions. Therefore, in this study, we employed a 633-nm laser, closely matching the energy level of the A exciton in MoS₂, as the excitation light source, serving as the resonance condition.

Under nonresonant excitation at 532 nm, the first-order Raman signals observed in both the monolayer and bilayer MoS₂ samples are the in-plane phonon mode E_{2g} (ML ~ 383.3 cm⁻¹, BL ~ 381.6 cm⁻¹) and the out-of-plane phonon mode A_{1g} (ML ~ 402.6 cm⁻¹, BL ~ 406.5 cm⁻¹). Conversely, the resonance Raman spectra of MoS₂ exhibits additional Raman peaks, namely the b mode (~418 cm⁻¹) and 2LA (~460 cm⁻¹), which arise from the DRR process. Increasing the number of layers in MoS₂ also leads to an increase in the separation between the E_{2g} and A_{1g} peaks.

As shown in Figs. 1(f) and 1(g), the peak separation for monolayer MoS₂ is 19.3 cm⁻¹, while for bilayer MoS₂, it is 24 cm⁻¹. The first-order of silicon Raman peak (F_{2g}) in both 532 nm and 633 nm excitations are located at 520 cm⁻¹. Both nonresonant and resonant Raman spectra have revealed a strong correlation between the phonon features in MoS₂ and the energy of the excitation light. Electrons excited by different photon energies follow distinct transition pathways, determining multiple possibilities for phonon energies [20]. By employing different polarized excitation and simultaneously analyzing the polarization states of the signal, we can distinguish the degeneracy of the signal and unveil the physical characteristics hidden beneath exciton-phonon interaction.

We employed different energy levels of the light sources to select nonresonant and resonant excitation conditions. By utilizing the polarization properties of the scattered light (linear and circular polarization), we conducted further analyses of the phonon symmetry from the polarization-resolved Raman spectra of MoS₂. This approach allowed us to observe the polarized behavior of Raman scattered light under different excitation conditions. To effectively showcase a dependable and consistent polarized Raman signal, a bilayer sample is employed to vividly illustrate various scenarios of exciton-phonon coupling strength. Figures 2(a) and 2(c) show the orthogonal polarized Raman spectra for the E_{2g} and A_{1g} in bilayer MoS₂, and F_{2g} in silicon under 532 nm and 633 nm excitation conditions with vertical linearly polarized light. The first symbol “V” indicates vertically polarized excitation, and the second symbol “V/H” denotes the polarization direction of the scattered light as either vertical or horizontal. Figures 2(b) and 2(d) display the orthogonal polarized Raman spectra under 532 nm and 633 nm excitation conditions with circularly polarized light. The first symbol σ₊ represents left circular polarized excitation, and the second symbol σ₊/σ₋ signifies the polarization direction of the scattered light as either left or right circular polarization. Under nonresonant vertical linearly polarized excitation, E_{2g} exhibits isotropic characteristics [Fig. 2(a)] because of the presence of two degenerate in-plane phonon modes (iTO and iLO) along two orthogonal directions. As a result, the Raman scattered light, when examined in terms of polarization, displays an isotropic distribution in the polar plot, as shown in the first diagram in Fig. 2(e). When a resonant excitation near the optical bandgap of MoS₂ is used, the Raman scattered light from E_{2g} becomes linearly polarized state in the same direction as the excitation light [see the first diagram in Fig. 2(f)]. This change is attributed to the efficient generation of excitons under resonant excitation, leading to a modulate coupling with LO phonons. In this condition, the intravalley scattering process resulting from the FI governs the alteration in the hidden phonon symmetry and is behind the change in the polarization of Raman scattered light, causing the in-plane degenerate phonons to a transition from the original symmetric to asymmetric states. This phenomenon has been discussed in the literature [21,22,28]. However, the Raman scattered light of A_{1g} mode remains in a linearly polarized state along the same direction as incident light and is unaffected by FI. This is a result of the weak coupling strength between phonons in the out-of-plane direction and excitons/electrons in the in-plane direction.

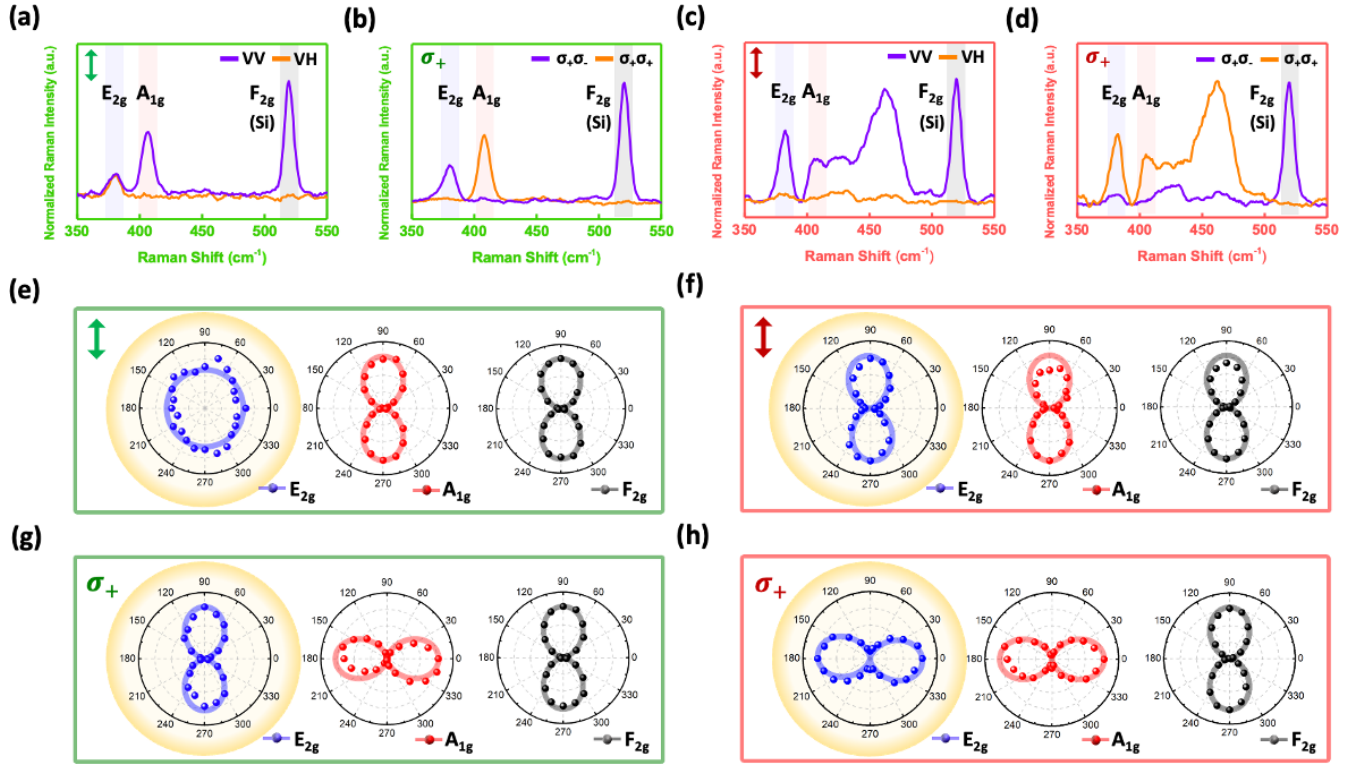


FIG. 2. Polarization-resolved Raman spectra of bilayer MoS₂ excited by nonresonant (marked in green) and resonant (marked in red) excitation. [(a), (b)] Nonresonant Raman spectra excited by linearly and circularly polarized light and detected by parallel (VV, $\sigma_+\sigma_+$) and crossed (VH, $\sigma_+\sigma_-$) polarization. [(c), (d)] Resonant Raman spectra excited by linearly and circularly polarized light and detected by parallel (VV, $\sigma_+\sigma_+$) and crossed (VH, $\sigma_+\sigma_-$) polarization. [(e)–(h)] Raman intensity polar plots of E_{2g} and A_{1g} in MoS₂, and F_{2g} in silicon corresponding to (a)–(d). The solid curves in (e)–(h) represent the numerical fittings for the experimental results.

In addition to linearly polarized excitation, the use of circularly polarized light with spin angular momentum as the excitation source is advantageous for investigating the phonon symmetry manifested in the polarization-resolved Raman spectra. This approach allows for a more comprehensive understanding of exciton-phonon coupling under the condition of angular momentum conservation. Under non-resonant excitation conditions, using left circularly polarized light, the degenerate E_{2g} phonon mode, due to material symmetry and conservation of angular momentum, can absorb left circularly polarized light and emit it with opposite angular momentum, allowing us to measure right circularly polarized Raman scattered light [Fig. 2(g)] [32–34]. However, under the resonant excitation, the dominant FI because of modulated exciton-phonon coupling leads to a change in the symmetry of the E_{2g} phonon mode, causing Raman scattered light to maintain a circular polarization state with the same helicity as the excitation light [Fig. 2(h)]. However, the out-of-plane A_{1g} phonon mode exhibits characteristic phonon features under circularly polarized excitation consistent with its structural symmetries, and remains unaffected by variations in energy excitation. In this analysis, we investigate the polarization of Raman scattering in MoS₂ when excited by linearly and circularly polarized light sources. Numerical calculation are carried out using Raman tensors and Jones calculus based on the computed Raman intensity formula [33,35],

$$I \propto \sum_n |\hat{\epsilon}_s(\theta) \cdot R_n \cdot \hat{\epsilon}_i|^2, \quad (1)$$

where R_n is the Raman tensor with the number of phonon modes n , $\hat{\epsilon}_i$ and $\hat{\epsilon}_s(\theta)$ are the unit vectors of polarized incident and scattered light, respectively. The Jones vector of the incident and scattered light can be represented as

$$\hat{\epsilon}_i = \begin{pmatrix} E_x e^{i\phi_x} \\ E_y e^{i\phi_y} \\ 0 \end{pmatrix} \quad (2)$$

and

$$\hat{\epsilon}_s(\theta) = (\cos \theta \quad \sin \theta \quad 0), \quad (3)$$

where E_x , E_y and ϕ_x , ϕ_y represent the amplitudes and phases of the electric field along x and y directions, respectively. θ is the transmission angle of the polarizer displayed in Fig. 1(a).

The Raman tensors of the E_{2g}, A_{1g}, and silicon (F_{2g}) are shown in Table I. The FI provides the additional diagonal term f parameter of the E_{2g} Raman tensor in MoS₂, which does not affect the A_{1g} mode [36]. Solid lines in Figs. 2(e)–2(h) represent the numerical results, showing a strong agreement with experimental data. Details of the computational parameters can be found in Table S1 within the SM [29].

The polarized Raman spectra of monolayer MoS₂ are displayed in Fig. S2 within the SM [29], and shows a similar trend to those of bilayer MoS₂ (see Fig. 2), indicating that in the case of fewer layers, phonon symmetry is independent of layers. Figure S2 within the SM [29] presents the results of measurements conducted at 77 K under both nonresonant and resonant excitations [29]. These results demonstrate that

TABLE I. Raman tensors of MoS₂ and silicon for E_{2g}, A_{1g}, and F_{2g} [21,22,36–40].

	MoS ₂ (E _{2g})	MoS ₂ (A _{1g})	Silicon (in [001]) (F _{2g})
Raman tensors	$R_{1(iTo)} = \begin{pmatrix} d_1 & 0 & 0 \\ 0 & -d_1 & 0 \\ 0 & 0 & 0 \end{pmatrix}$	$R_{1(oZo)} = \begin{pmatrix} a_1 & 0 & 0 \\ 0 & a_1 & 0 \\ 0 & 0 & b_1 \end{pmatrix}$	$R_{1(F_{2g1})} = \begin{pmatrix} 0 & 0 & d_2 \\ 0 & 0 & 0 \\ -d_2 & 0 & 0 \end{pmatrix}$
	$R_{2(iLo)} = \begin{pmatrix} f & d_1 & 0 \\ d_1 & f & 0 \\ 0 & 0 & f \end{pmatrix}$		$R_{2(F_{2g2})} = \begin{pmatrix} 0 & 0 & 0 \\ 0 & 0 & d_2 \\ 0 & d_2 & 0 \end{pmatrix}$
			$R_{3(F_{2g3})} = \begin{pmatrix} -d_2 & 0 & 0 \\ 0 & d_2 & 0 \\ 0 & 0 & 0 \end{pmatrix}$

the symmetry of the first-order Raman E_{2g} and A_{1g} phonon modes remain unaffected with temperature variations. The additional experimental data for the Raman peak positions and the corresponding temperature-dependent Raman spectra are shown in Fig. S3 within the SM [29]. These Raman peak positions, along with the well-fitted linear data, indicate lattice contraction as temperature decreases.

To gain a clearer understanding of the temperature-dependent interaction between electrons and excitons in first-order and second-order Raman scattering, a phenomenological mechanism of exciton-phonon coupling strength at different laser excitations and temperatures is proposed. The results for polarized Raman spectra, under nonresonant conditions, indicate that when the excitation energy exceeds the exciton energy, the strength of the exciton-phonon coupling during the electron transition process is weak. The overall potential energy of MoS₂ is predominantly governed by the deformation potential (DP), as illustrated in the schematic band diagram in Fig. 3(a). The DP in 2D materials, reflecting the energy change of electronic states in response to atomic displacements from lattice vibrations (phonons), significantly influences electron-phonon coupling. This allows for further investigation of the electron-phonon interaction in the Raman tensors analyses [41–43]. Additionally, as shown in Fig 3(a), when MoS₂ is illuminated with left circular polarized light, the polarized scattered light of the Raman active E_{2g} phonon mode follows the symmetry of the MoS₂ lattice under the influence of the DP, exhibiting helicity-exchanged possess right circular polarization.

When MoS₂ material is subjected to resonant excitation, the exciton-phonon coupling strength during the electron transition process is stronger compared to the nonresonant condition. Consequently, the DRR scattering phenomenon arises, as illustrated in the band diagram (red dashed line) shown in Fig. 3(b). In parallel, it triggers the generation of phonons, specifically the b mode, resulting from the interaction of two phonon modes within the K and K' valleys of the Brillouin zone [20]. In this context, the FI becomes the dominant factor in determining the overall potential energy of MoS₂, leading to the helicity preserved of the E_{2g} phonon mode shown in Fig. 2. This reflects the close relation between phonon symmetry and exciton-phonon coupling strength. Furthermore, the scattered light of the b mode also exhibits specific polarization characteristics, with the left circular polarization intensity greater than right circular polarization

intensity. As the 2LA mode consists of multiple phonons, creating a complex configuration, we do not discuss the polarization characteristics of the scattered light in this paper.

As the temperature decreases, monolayer MoS₂ exhibits higher valley polarization under resonant excitation. In Fig. 3, the arrow colors representing excitons indicate left-handed (blue) and right-handed (yellow) circularly polarized light, while the number of arrows reflects the number of photons. There is a trend of increasing degree of circular polarization of excitons from 300 K to 77 K, which is more pronounced under resonant excitation conditions. This implies that the electronic transition pathway becomes more confined to precise energy level, as illustrated by the strong exciton-phonon coupling condition in Fig. 3(d). At low temperature, the dominance of exciton-phonon coupling over electron-phonon coupling becomes evident, especially when the exciton energy levels closely align with the laser excitation energy. This alignment leads to resonance enhancement and a heightened influence of the FI across the system. Therefore, the strong exciton-phonon coupling strength in monolayer MoS₂ subjected to low-temperature resonant excitation is associated with the level of valley polarization in excitons and the symmetry of b mode. As depicted in Fig. 3(d), it elucidates the helicity transformation mechanism in the circular polarization properties of the b mode with the increase in exciton valley polarization at reduced temperatures. In contrast, Fig. 3(c) depicts the nonresonant excitation condition, where electrons are excited to higher energy levels, resulting in lower valley polarization, indicative of weak exciton-phonon coupling strength. Therefore, at low temperature under nonresonant excitation, the symmetry of the E_{2g} phonon mode remains consistent with that at room temperature. Subsequently, we will investigate the polarization characteristics of the DRR scattered light as the temperature gradually decreases, concurrent with an increasing FI.

Through the analysis of polarization-resolved Raman spectra for monolayer and bilayer MoS₂ at various temperatures, variations in the exciton-phonon coupling strength between direct and indirect band gaps can be observed. Figure 4 shows the temperature-dependent polarized Raman spectra of monolayer and bilayer MoS₂ under resonant excitation. When circularly polarized light is used as the excitation and the temperature is reduced from 300 K to 77 K, the polarization states of most Raman active modes remain unchanged. However, an exception is observed in the case of the b mode, which exhibits

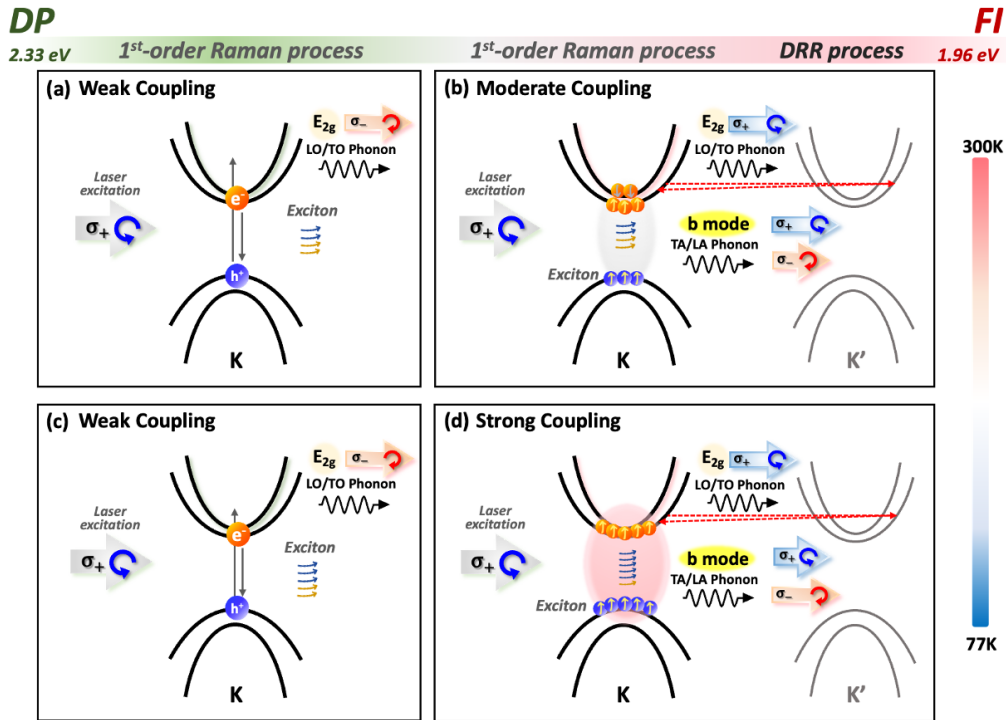


FIG. 3. Schematic band diagram illustrating exciton and phonon characteristics in MoS₂, showcasing their variations with changing temperature and excitation energy. (a) Weak-coupling condition of nonresonant excitation at 300 K. (b) Moderate-coupling condition of resonant excitation at 300 K, (c) Weak-coupling condition of nonresonant excitation at 77 K, (d) Strong-coupling condition of resonant excitation at 77 K. The colors (blue and yellow) and the number of arrows for excitons represent the schematic degree of circular polarization of photoluminescence intensity behavior. The red-dashed line indicates the schematic of DRR process with TA/LA phonon b mode.

an opposing trend. Specifically, the b mode undergoes a transition from helicity-preserved to helicity-exchanged, as shown in Figs. 4(a) and 4(b) (marked with the yellow bar). To clearly illustrate the temperature-dependent Raman spectra, Figs. 4(c)

and 4(d) demonstrate polarization-resolved mappings of bilayer MoS₂ at 300 K and 77 K. These maps provide a clear visualization of the chirality transition of the b mode. We further calculated the degree of circular polarization (DoCP)

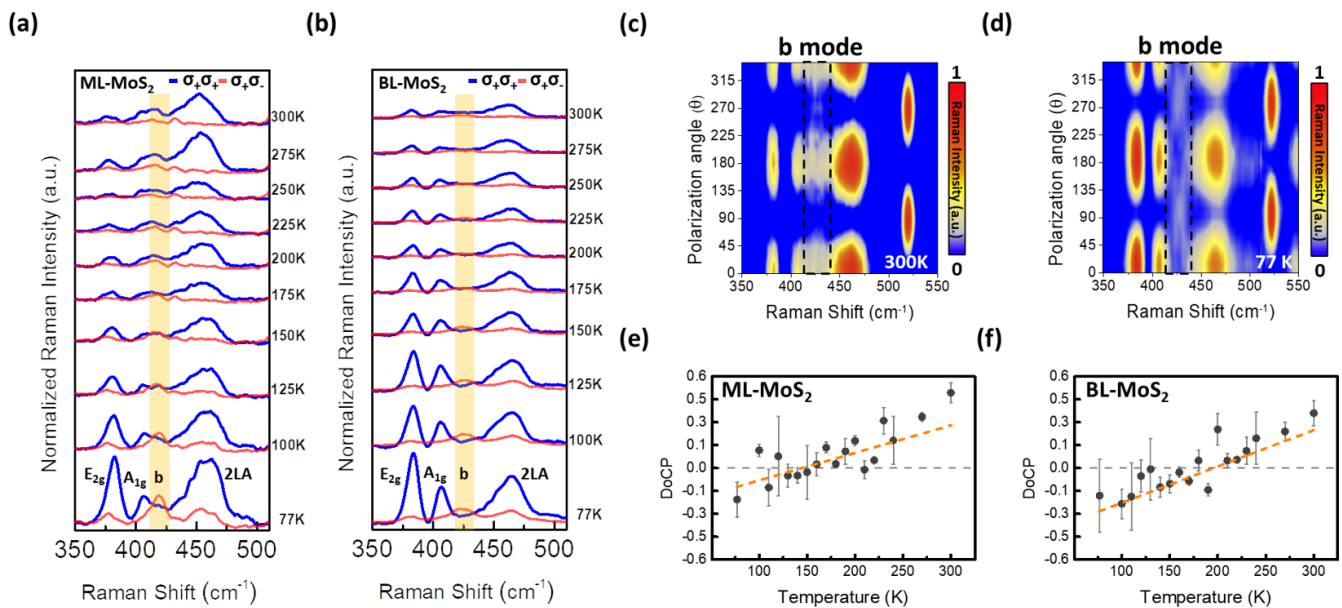


FIG. 4. Temperature-dependent polarized Raman spectra of (a) monolayer and (b) bilayer MoS₂ excited by circularly polarized resonant excitation (633 nm). (c) Polarized Raman intensity mapping of bilayer MoS₂ measured at 300 K and (d) 77 K. The polarization angle (θ) represents the orientation of the polarizer placed in front of the spectrometer. (e) Degree of circular polarization (DoCP) values with linear fit of b mode in monolayer MoS₂ and (f) bilayer MoS₂.

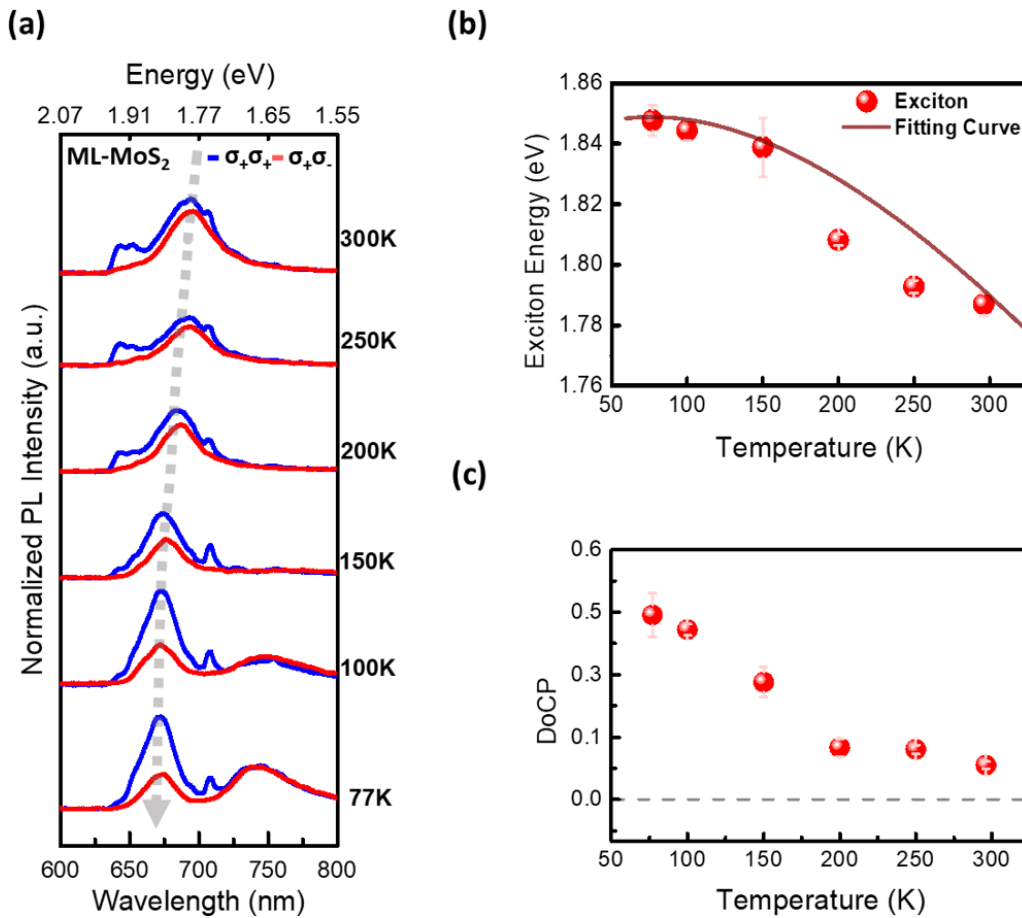


FIG. 5. (a) Temperature-dependent polarized PL spectra of monolayer MoS₂ excited by circularly polarized resonant light. The gray-dashed line is a guide-to-the-eye curve for the blue-shifted peak position with decreasing temperature. The additional peak presence in PL spectra around 707 nm is the peak of He-Ne laser in our system (Fig. S6 within the SM [29]). (b) Exciton peak positions with Varshni formula fitting curve. (c) Degree of circular polarization (DoCP) values extracted from the exciton shown in (a).

of the Raman scattered light associated with the b mode at various temperatures for monolayer and bilayer MoS₂, as shown in Figs. 4(e) and 4(f). The DoCP is defined as $\frac{I_{\sigma_+ \sigma_+} - I_{\sigma_+ \sigma_-}}{I_{\sigma_+ \sigma_+} + I_{\sigma_+ \sigma_-}}$, where a value of 1 represents pure helicity-preserve, while value of -1 represents pure helicity-exchange. With decreasing temperature from 300 K to 77 K, the chirality of the b mode transitions from around 0.45 helicity-preserved to gradually become around -0.15 helicity-exchanged corresponding to the stronger exciton-phonon coupling phenomena [Fig. 3(d)]. The transition temperatures for the b mode chirality in monolayer and bilayer MoS₂ are approximately 150 K and 190 K, respectively. The b mode Raman intensity polar plots extracted from polarized Raman intensity mapping results are shown in Fig. S4 within the SM [29]. At 300 K, the polarization state of the b mode in monolayer and bilayer MoS₂ remains helicity-preserved, with respective DoCP values of 0.71 and 0.43, displaying dumbbell-shaped polar plots. Moreover, as the temperature decreases, the DoCP values for monolayer and bilayer MoS₂ are -0.07 and -0.13 , respectively, indicating helicity-exchanged polarization states and circle-like shapes in the polar plots. We additionally performed temperature-dependent polarized Raman spectra on bulk MoS₂, illustrated in Fig. S5 within the

SM [29]. In light of the indirect bandgap nature and the absence of PL intensity in bulk MoS₂, the exciton-phonon coupling is very weak, resulting in unchanged chirality of the b mode.

In the resonant condition where the excitation energy approaches the MoS₂ bandgap, the permissible electron transition pathways become more constrained. This limitation also imposes restrictions on the electron spin states, consequently enhancing the degree of valley polarization. This enhancement is manifested in the circular polarization of PL emitted during electron-hole recombination. Under this condition, polarized Raman spectra exhibit corresponding effects attributed to the pronounced exciton-phonon coupling. Hence, we conducted measurements of MoS₂ PL circular polarization across different temperatures to clarify its correlation with temperature-dependent circularly polarized Raman spectra. Figure 5 depicts the temperature-dependent polarized PL spectra of monolayer MoS₂. When left circular polarized light is used as the excitation, the examination of the left and right circular components of the PL signal reveals the degree of valley polarization, as shown in Fig. 5(a), as the temperature decreases from 300 K to 77 K. The exciton peak at 685 nm signifies the optical band gap (~ 1.81 eV) at K point in monolayer MoS₂. The peak position exhibits a blue-shift phenomenon as

the temperature decreases. Additionally, when the temperature drops to around 100 K, a localized exciton peak emerges at 745 nm, which is out of the scope of discussion in this paper. Figures 5(b) and 5(c) present the results of the energy gap extracted from the PL peak position and the DoCP variation with temperature. In semiconductors, the variation of optical band gap in PL peak as a function of the temperature (T) can be fitted by the Varshni equation,

$$E_g(T) = E_0 - \frac{\alpha T^2}{T + \beta}, \quad (4)$$

where $E_g(T)$ represents the energy gap for direct band gap, E_0 is the energy gap at 0 K, and α and β are the constant values denoting the entropy as T approaches infinity and Debye temperature, respectively [44,45]. We have employed the Varshni equation to fit the peak position shifting with temperature, yielding good results as indicated by the solid line in Fig. 5(b). The valley polarization of monolayer MoS₂ increases as the temperature decreases, with the DoCP rising from 0.1 at 300 K to 0.45 at 77 K. MoS₂ exhibits heightened valley polarization under resonant excitation, indicating a more confined electronic transition pathway at precise energy levels, correlating to the chirality transition of the b mode. The experimental results demonstrate that temperature variations affect the phonon symmetry of the b mode in both monolayer and bilayer MoS₂, while also influencing the degree of valley polarization detected by polarization-resolved PL measurement. When considering bulk MoS₂ with an indirect band gap and without PL, the symmetry of the b mode is relatively less affected by temperature. These findings lead to the conclusion that the strength of exciton-phonon coupling in MoS₂ depends on its band structure and temperature, as well as its b mode symmetry, showing a strong correlation with valley polarization. The consistency of experimental results further validates the proposed mechanism in Fig. 3.

IV. CONCLUSIONS

In summary, this study systematically investigated the relation between phonon symmetry, exciton-phonon coupling, and valley polarization in MoS₂ under various temperature conditions and excitations. Through the use of nonresonant and resonant excitations, as well as the polarization properties of light, the results clarify the influence of exciton-phonon coupling strength on Raman scattered light polarization. Specifically, in the in-plane E_{2g} mode, distinct Raman scattered light polarization characteristics are exhibited, influenced by the DP and the FI, respectively. Furthermore, an increase in valley polarization at lower temperatures, along with the helicity transition in the DRR b mode, underscores the significance of strong exciton-phonon coupling. By employing polarization analysis of light, these unique exciton-phonon coupling phenomena are elucidated. This research significantly advances our understanding of the optoelectronic properties of MoS₂ and provides valuable insights for applications in the field of 2D semiconductor materials.

ACKNOWLEDGMENTS

This work was supported by the National Science and Technology Council (NSTC) of Taiwan under Contract NSTC 112–2112-M-003–014 and NSTC 111–2628-M-003–002-MY3.

Y.-C. Chang and Y.-C. Chan performed the experiments. B.D., J.-F.S., and Y.-C. Chang performed the numerical calculations and joined the discussion of the experimental results and numerical analyses. H.-C.H. prepared MoS₂ sample. T.-H.L. and Y.-W.L. supervised the research. All authors discussed the results and commented on the manuscript.

The authors declare no competing financial interests.

-
- [1] Q. H. Wang, K. Kalantar-Zadeh, A. Kis, J. N. Coleman, and M. S. Strano, Electronics and optoelectronics of two-dimensional transition metal dichalcogenides, *Nat. Nanotechnol.* **7**, 699 (2012).
- [2] R. Ganatra and Q. Zhang, Few-layer MoS₂: A promising layered semiconductor, *ACS Nano* **8**, 4074 (2014).
- [3] Y. Zhou, H. Yin, and S. Ai, Applications of two-dimensional layered nanomaterials in photoelectrochemical sensors: A comprehensive review, *Coord. Chem. Rev.* **447**, 214156 (2021).
- [4] Q. Fu, J. Han, X. Wang, P. Xu, T. Yao, J. Zhong, W. Zhong, S. Liu, T. Gao, and Z. Zhang, 2D transition metal dichalcogenides: Design, modulation, and challenges in electrocatalysis, *Adv. Mater.* **33**, 1907818 (2021).
- [5] B. Radisavljevic, A. Radenovic, J. Brivio, V. Giacometti, and A. Kis, Single-layer MoS₂ transistors, *Nat. Nanotechnol.* **6**, 147 (2011).
- [6] B. Chakraborty, A. Bera, D. V. S. Muthu, S. Bhowmick, U. V. Waghmare, and A. K. Sood, Symmetry-dependent phonon renormalization in monolayer MoS₂ transistor, *Phys. Rev. B* **85**, 161403(R) (2012).
- [7] A. Newaz, D. Prasai, J. I. Ziegler, D. Caudel, S. Robinson, R. F. Haglund Jr, and K. I. Bolotin, Electrical control of optical properties of monolayer MoS₂, *Solid State Commun.* **155**, 49 (2013).
- [8] D. Lembke, S. Bertolazzi, and A. Kis, Single-layer MoS₂ electronics, *Acc. Chem. Res.* **48**, 100 (2015).
- [9] X. Lu, M. I. B. Utama, X. Wang, W. Xu, W. Zhao, M. H. S. Owen, and Q. Xiong, Gate-tunable resonant Raman spectroscopy of bilayer MoS₂, *Small* **13**, 1701039 (2017).
- [10] S. Mitra, D. Srivastava, S. S. Singha, S. Dutta, B. Satpati, M. Karppinen, A. Ghosh, and A. Singha, Tailoring phonon modes of few-layered MoS₂ by in-plane electric field, *npj 2D Mater. Appl.* **4**, 6 (2020).
- [11] Y. Yoon, K. Ganapathi, and S. Salahuddin, How good can monolayer MoS₂ transistors be? *Nano Lett.* **11**, 3768 (2011).
- [12] G. Kukucska and J. Koltai, Theoretical investigation of strain and doping on the Raman spectra of monolayer MoS₂, *Physica Status Solidi (b)* **254**, 1700184 (2017).
- [13] M. Xia, A review on applications of two-dimensional materials in surface-enhanced Raman spectroscopy, *Spectrosc.: Int. J.* **2018**, 4861472 (2018).
- [14] M. W. Iqbal, K. Shahzad, R. Akbar, and G. Hussain, A review on Raman finger prints of doping and strain effect in TMDCs, *Microelectron. Eng.* **219**, 111152 (2020).

- [15] Z. Lin, W. Liu, S. Tian, K. Zhu, Y. Huang, and Y. Yang, Thermal expansion coefficient of few-layer MoS₂ studied by temperature-dependent Raman spectroscopy, *Sci. Rep.* **11**, 7037 (2021).
- [16] S. Golovynskyi, I. Irfan, M. Bosi, L. Seravalli, O. I. Datsenko, I. Golovynska, B. Li, D. Lin, and J. Qu, Exciton and trion in few-layer MoS₂: Thickness- and temperature-dependent photoluminescence, *Appl. Surf. Sci.* **515**, 146033 (2020).
- [17] H. Li and X. Zhang, Temperature-dependent photoluminescence and time-resolved photoluminescence study of monolayer molybdenum disulfide, *Opt. Mater.* **107**, 110150 (2020).
- [18] M. Bhatnagar, T. Woźniak, Ł. Kipczak, N. Zawadzka, K. Olkowska-Pucko, M. Grzeszczyk, J. Pawłowski, K. Watanabe, T. Taniguchi, and A. Babiński, Temperature induced modulation of resonant Raman scattering in bilayer 2H-MoS₂, *Sci. Rep.* **12**, 14169 (2022).
- [19] B. R. Carvalho, L. M. Malard, J. M. Alves, C. Fantini, and M. A. Pimenta, Symmetry-dependent exciton-phonon coupling in 2D and bulk MoS₂ observed by resonance Raman scattering, *Phys. Rev. Lett.* **114**, 136403 (2015).
- [20] B. R. Carvalho, Y. Wang, S. Mignuzzi, D. Roy, M. Terrones, C. Fantini, V. H. Crespi, L. M. Malard, and M. A. Pimenta, Intervalley scattering by acoustic phonons in two-dimensional MoS₂ revealed by double-resonance Raman spectroscopy, *Nat. Commun.* **8**, 14670 (2017).
- [21] B. Miller, J. Lindlau, M. Bommert, A. Neumann, H. Yamaguchi, A. Holleitner, A. Högele, and U. Wurstbauer, Tuning the Fröhlich exciton-phonon scattering in monolayer MoS₂, *Nat. Commun.* **10**, 807 (2019).
- [22] Y. Zhao, S. Zhang, Y. Shi, Y. Zhang, R. Saito, J. Zhang, and L. Tong, Characterization of excitonic nature in Raman spectra using circularly polarized light, *ACS Nano* **14**, 10527 (2020).
- [23] J. Chen and C. Wang, Second order Raman spectrum of MoS₂, *Solid State Commun.* **14**, 857 (1974).
- [24] G. L. Frey, R. Tenne, M. J. Matthews, M. S. Dresselhaus, and G. Dresselhaus, Raman and resonance Raman investigation of MoS₂ nanoparticles, *Phys. Rev. B* **60**, 2883 (1999).
- [25] J. Kutrowska-Girzycka, J. Jadczyk, and L. Bryja, The study of dispersive 'b'-mode in monolayer MoS₂ in temperature dependent resonant Raman scattering experiments, *Solid State Commun.* **275**, 25 (2018).
- [26] B. R. Carvalho and M. A. Pimenta, Resonance Raman spectroscopy in semiconducting transition-metal dichalcogenides: Basic properties and perspectives, *2D Mater.* **7**, 042001 (2020).
- [27] R. Rao, R. A. Yadav, N. Padma, J. Jagannath, and A. Arvind, Investigation of electron-phonon interaction in bulk and nanoflakes of MoS₂ using anomalous "b" mode in the resonant Raman spectra, *J. Appl. Phys.* **128**, 165703 (2020).
- [28] H. Fröhlich, Interaction of electrons with lattice vibrations, *Proc. R. Soc. London, Ser. A* **215**, 291 (1952).
- [29] See Supplemental Material at <http://link.aps.org/supplemental/10.1103/PhysRevMaterials.8.074003> for sample images and polarization-resolved Raman spectra of monolayer and bilayer MoS₂ excited by 532 nm and 633 nm excitation;
- (i) Polarization-resolved Raman spectra of monolayer MoS₂ excited by 532 nm and 633 nm excitation; (ii) Temperature-dependent Raman spectra of monolayer MoS₂ and bilayer MoS₂; (iii) Raman intensity polar plots of b mode with calculated DoCP value excited by circularly polarized resonant excitation (633 nm); (iv) Temperature-dependent polarized Raman spectra of bulk MoS₂ excited by circularly polarized resonant excitation (633 nm); (v) Temperature-dependent polarized PL spectra of monolayer MoS₂ excited by circularly polarized resonant light.
- [30] H.-L. Liu, T. Yang, J.-H. Chen, H.-W. Chen, H. Guo, R. Saito, M.-Y. Li, and L.-J. Li, Temperature-dependent optical constants of monolayer MoS₂, MoSe₂, WS₂, and WSe₂: Spectroscopic ellipsometry and first-principles calculations, *Sci. Rep.* **10**, 15282 (2020).
- [31] L. Vinna, S. Logothetidis, and M. Cardona, Temperature dependence of the dielectric function of germanium, *Phys. Rev. B* **30**, 1979 (1984).
- [32] S.-Y. Chen, C. Zheng, M. S. Fuhrer, and J. Yan, Helicity-resolved Raman scattering of MoS₂, MoSe₂, WS₂, and WSe₂ atomic layers, *Nano Lett.* **15**, 2526 (2015).
- [33] Y. Tatsumi and R. Saito, Interplay of valley selection and helicity exchange of light in Raman scattering for graphene and MoS₂, *Phys. Rev. B* **97**, 115407 (2018).
- [34] L. Zhang and Q. Niu, Chiral phonons at high-symmetry points in monolayer hexagonal lattices, *Phys. Rev. Lett.* **115**, 115502 (2015).
- [35] R. Loudon, Theory of the resonance Raman effect in crystals, *J. Phys.* **26**, 677 (1965).
- [36] A. Cantarero, C. Trallero-Giner, and M. Cardona, Excitons in one-phonon resonant Raman scattering: Fröhlich and interference effects, *Phys. Rev. B* **40**, 12290 (1989).
- [37] C. Trallero-Giner, A. Cantarero, and M. Cardona, One-phonon resonant Raman scattering: Fröhlich exciton-phonon interaction, *Phys. Rev. B* **40**, 4030 (1989).
- [38] A. Talochkin, Circularly polarized Raman scattering in silicon, *J. Raman Spectrosc.* **51**, 201 (2020).
- [39] J. Steele, P. Puech, and R. A. Lewis, Polarized Raman backscattering selection rules for (*hhl*)-oriented diamond and zincblende-type crystals, *J. Appl. Phys.* **120**, 055701 (2016).
- [40] X. Zhang, X.-F. Qiao, W. Shi, J.-B. Wu, D.-S. Jiang, and P.-H. Tan, Phonon and Raman scattering of two-dimensional transition metal dichalcogenides from monolayer, multilayer to bulk material, *Chem. Soc. Rev.* **44**, 2757 (2015).
- [41] J. Bardeen and W. Shockley, Deformation potentials and mobilities in non-polar crystals, *Phys. Rev.* **80**, 72 (1950).
- [42] F. Demangeot, J. Frandon, M. Renucci, O. Briot, B. Gil, and R.-L. Aulombard, Raman determination of phonon deformation potentials in α -GaN, *Solid State Commun.* **100**, 207 (1996).
- [43] A. K. Ganguly and J. L. Birman, Theory of lattice Raman scattering in insulators, *Phys. Rev.* **162**, 806 (1967).
- [44] Y. P. Varshni, Temperature dependence of the energy gap in semiconductors, *Physica* **34**, 149 (1967).
- [45] K. P. O'donnell and X. Chen, Temperature dependence of semiconductor band gaps, *Appl. Phys. Lett.* **58**, 2924 (1991).